SUPPORTING INFORMATION

Acetonyl Peroxy and Hydro Peroxy Self- and Cross- Reactions: Kinetics, Mechanism, and Chaperone Enhancement from the Perspective of the Hydroxyl Radical Product

Kristen Zuraski,[a] Aileen O. Hui,[b,c] Fred J. Grieman,[*,a,d] Emily Darby,[a,d,e] Kristian H. Møller,[f] Frank A. F. Winiberg,[a] Carl J. Percival,[a] Matthew D. Smarte,[b] Mitchio Okumura,[b] Henrik G. Kjaergaard,[*,f] and Stanley P. Sander[*,a]

[a]NASA Jet Propulsion Laboratory, California Institute of Technology, 4800 Oak Grove Drive, Pasadena, California 91109, United States

[b]Arthur Amos Noyes Laboratory of Chemical Physics, California Institute of Technology, Pasadena, California 91125, United States

[c]now at: The Aerospace Corporation, El Segundo, California 90245, United States

[d]Seaver Chemistry Laboratory, Pomona College, Claremont, California 91711, United States

[e]now at: Trussell Technologies, Oakland, California 94612, United States

[f]Department of Chemistry, University of Copenhagen, Universitetsparken 5, DK-2100 Copenhagen Ø, Denmark

Number of pages: S1-S15 **Number of Figures: 12** **Number of Tables: 2**

I. Instrumental Calibrations for $[HO_2]$, $[Cl]_0$, and [OH]

HO_2 Concentrations by IR-WMS and Starting Radical Concentrations

A near-infrared (NIR) diode laser operating in wavelength modulated spectroscopy (WMS) conditions monitored the $2\nu_1$ overtone O—H stretch of HO_2 at 6638.2 cm^{-1}.[1] The NIR laser was calibrated daily against UV (λ = 225 nm, $\sigma_{HO2}(225\ nm) = 2.4 \times 10^{-18}\ cm^2\ molecule^{-1}$) absorption measurements[2], where the wavelength was chosen to isolate HO_2 from other peroxy radicals. Four datasets (40 photolysis laser shots each) were obtained for different starting radical concentrations. Kinetic simulations (see main text) fit the UV and IR traces for each run where both representing the same $HO_2 + HO_2$ kinetics arising from the typical concentrations listed in Table S1 the set of reactions indicated in Table S2. The model accounted for absorption due to the resultant H_2O_2 product($\sigma_{H2O2}(225\ nm) = 2.17 \times 10^{-19}\ cm^2\ molecule^{-1}$). Fits determined the calibration factor for the NIR laser, $V_{M,NIR}$, and the initial radical concentration, $[Cl]_0$. The calibration factor was then used in all subsequent experiments to convert the NIR signal in mV, S_{NIR}, to HO_2 concentration using ES1.

$$[HO_2] = S_{NIR} \times V_{M,NIR} \quad \text{(ES1)}$$

Uncertainties in $V_{M,NIR}$, which were included in the MC calculations for determining the rate constants and branching ratios for the acetonyl peroxy self-reaction and acetonyl peroxy + HO_2 reaction, averaged 1.9% based on the standard deviation across multiple calibration runs. Figure S1a and S1b shows representative fits of the UV and IR traces, respectively, and Figure S2 shows the corresponding initial radical concentrations for four starting chlorine concentrations. The temperature and pressure for experiments were 298 K and 100 Torr, respectively.

OH Concentrations by IR-WMS

A mid-infrared (MIR) diode laser operating in WMS conditions, coaligned with the NIR laser through the flow cell, monitored the ν_1 fundamental stretch of OH at 3407.6 cm^{-1}.[1] The reaction between HO_2 + NO, where OH is formed in unity, was observed while simultaneously monitoring the time-dependent [HO_2] and [OH] concentrations with the NIR and MIR laser, respectively. Three datasets (40 photolysis laser shots each) were taken with different starting radical concentrations to determine the standard deviation for the calibration value. Results from [HO_2] and $[Cl]_0$ calibrations were used with the reactions listed in Table S2 to conduct kinetic simulations and fit the two experimental kinetic traces, shown in Figure S3, to determine the calibration factor for the MIR laser, $V_{M,MIR}$. Similar to the uncertainty in $V_{M,NIR}$, the uncertainty in $V_{M,MIR}$ averaged 2.3% based on the standard deviation across the calibration runs and this was propagated into the subsequent analysis for the rate constants and branching ratios reported in this work. The equation ES2 was then used in subsequent experiments.

$$[OH] = S_{MIR} \times V_{M,MIR} \quad \text{(ES2)}$$

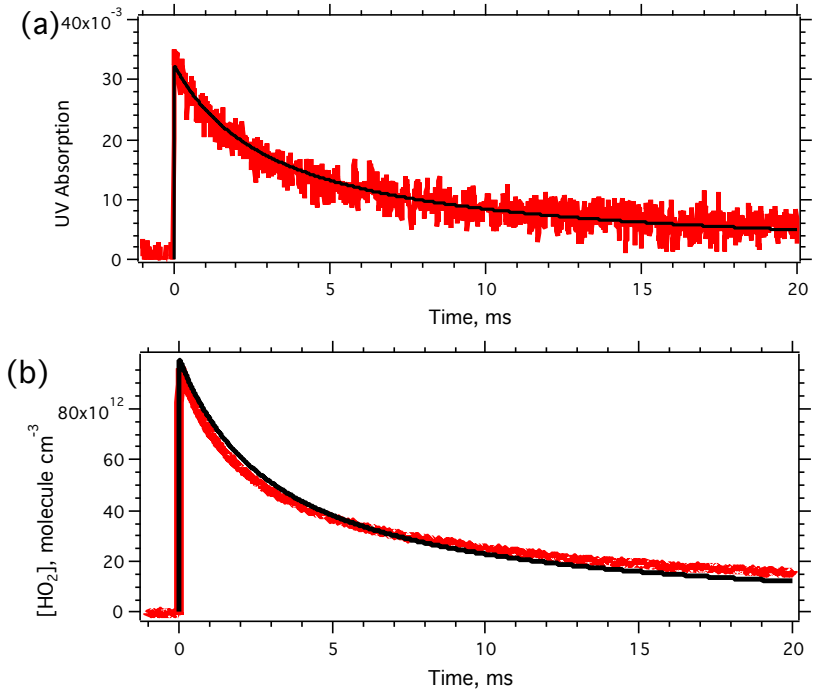

Figure S1. Typical fits of the IR and UV kinetic traces for the HO_2 + HO_2 reaction. T = 298 K, P = 100 Torr.

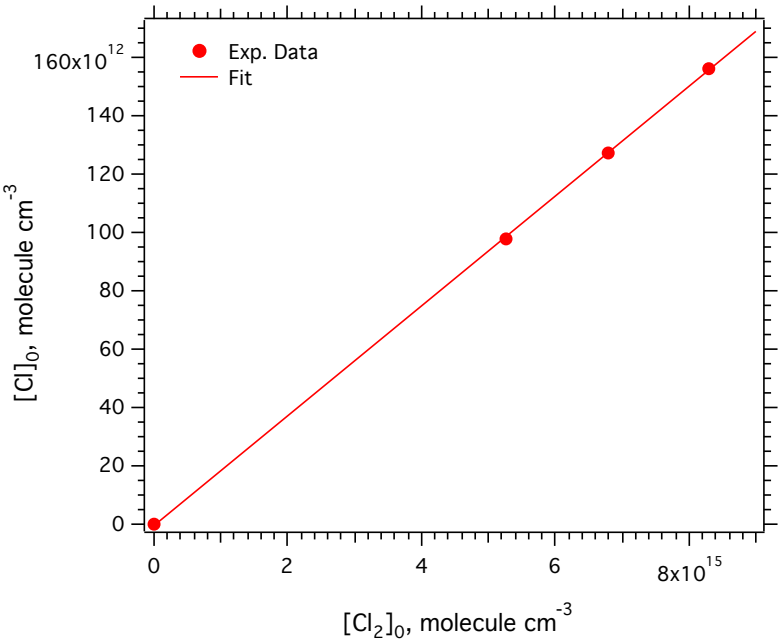

Figure S2. Typical starting radical concentration, $[Cl]_0$, vs. $[Cl_2]$ recorded at 110 mJ/pulse photolysis laser energy.

Table S1: Typical Concentrations for Calibration Experiments

Species	Concentration, molecule cm^{-3}
Cl_2	$5–9 \times 10^{15}$
CH_3OH	4×10^{15}
O_2	2×10^{18}
NO	1.1×10^{15}*

* [NO] = 0 for NIR calibration experiments.

Table S2. Reaction scheme used in the calibration of the NIR and MIR diode laser operating under WMS conditions. Rate coefficients are taken from the JPL Data Evaluation recommended values[2] with units in $molecules^{-1}\ cm^3\ s^{-1}$.

Reaction	Branching Ratio	Rate coefficient
Starting Radical Generation		
$CH_3OH + Cl \rightarrow CH_2OH + HCl$		5.5×10^{-11}
$CH_2OH + O_2 \rightarrow HO_2 + CH_2O$		9.1×10^{-12}
HO_x Chemistry for NIR and MIR Laser Calibration		
$HO_2 + HO_2 \rightarrow H_2O_2 + O_2$		$3\times10^{-13}\ exp(460/T) + M \times 2.1\times10^{-33}\ exp(920/T)$
$Cl + HO_2 \rightarrow OH + ClO$		$3.6 \times 10^{-11}\ exp(-375/T)$
$Cl + HO_2 \rightarrow O_2 + HCl$		$1.4 \times 10^{-11}\ exp(270/T)$
$HO_2 + CH_2O \rightarrow HOCH_2O_2$		$6.7 \times 10^{-15}\ exp(600/T)$
Additional HO_x and NO_x Chemistry for MIR Calibrations		
$HO_2 + NO \rightarrow NO_2 + OH$		$3.3 \times 10^{-12}\ exp(270/T)$
$OH + CH_3OH \rightarrow CH_2OH + H_2O$	0.85	$2.9 \times 10^{-12}\ exp(-345/T)$
$OH + CH_3OH \rightarrow CH_3O + H_2O$	0.15	
$CH_3O + O_2 \rightarrow CH_2O + HO_2$		$3.9 \times 10^{-14}\ exp(-900/T)$
$OH + CH_2O \rightarrow H_2O + HCO$		$5.5 \times 10^{-12}\ exp(125/T)$
$OH + OH \rightarrow H_2O + O$		1.8×10^{-12}
$OH + OH\ (+M) \rightarrow H_2O_2$		5.03×10^{-31} [M]
$OH + HO_2 \rightarrow H_2O + O_2$		$4.8 \times 10^{-11}\ exp(250/T)$
$OH + HCl \rightarrow H_2O + Cl$		$1.8 \times 10^{-12}\ exp(-250/T)$
$OH + NO_2 \rightarrow HONO_2$		3.59×10^{-12}

$OH + NO_2 \rightarrow HOONO$	2.94×10^{-13}
$OH + NO \rightarrow HONO$	1.84×10^{-12}
$HO_2 + NO_2 \rightarrow HO_2NO_2$	4.19×10^{-13}
$OH + HONO \rightarrow H_2O + NO_2$	$1.8 \times 10^{-11} \exp(-390/T)$
$OH + Cl_2 \rightarrow HOCl + Cl$	$2.6 \times 10^{-12} \exp(-1100/T)$
$HCO + O_2 \rightarrow HO_2 + CO$	5.2×10^{-12}

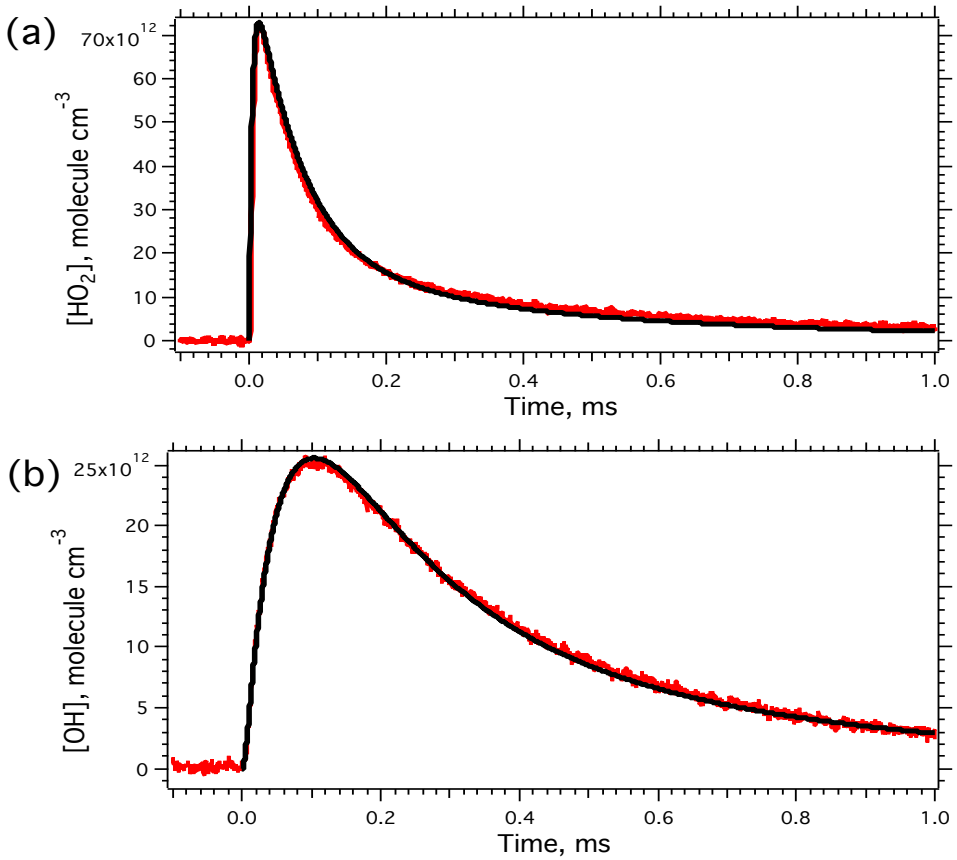

Figure S3. Typical fits (black) for time dependent (a) HO_2 and (b) OH concentrations (red) from the reaction HO_2 + NO data. T = 298 K, P = 100 Torr.

II. Details of the RRKM-ME Modelling

The reactions outlined in Figure 11 in the main manuscript are modelled using the Rice-Ramsperger-Kassel-Marcus Master Equation approach implemented in the Master Equation Solver for Multi Energy-well Reactions (MESMER). Energetics are calculated for the lowest-energy conformers at the RO-CCSD(T)-F12a/VDZ-F12//ωB97X-D/aug-cc-pVTZ level with

ωB97X-D/aug-cc-pVTZ zero-point vibrational energies (ZPVE), see Figure S3. The following parameters are used in the modelling:

- T = 298.15 K and P = 100 Torr.
- Exponential energy transfer with an average transfer pr. collision of $\Delta E_{down} = 300\ \mathrm{cm^{-1}}$, as found to be suitable for ethylamine which is of comparable size to the species studied here.[3, 4]
- Lennard-Jones parameters corresponding to those of hydrocarbons of similar size as reported by Hippler et al.[5]
- Rate coefficient for the reaction of alkyl radicals with O_2 of $k(\mathrm{R} + \mathrm{O_2}) = 1.9 \cdot 10^{-13}$ cm^3 molecule^{-1} s^{-1} corresponding to k_{4a} in Table 1 in the main manuscript at 298.15 K.
- $[O_2] = 1.6 \cdot 10^{18}$ molecule cm^{-3} as typical for the experiments.
- Grain size of 50 cm^{-1} and energy grain span above the highest stationary point (energy above the top hill) of 50k_BT.
- Bath gas = N_2 (σ = 3.919 Å, ε/k_B = 91.85 K).[6]
- Products are modelled as sinks.

Surprisingly, the MESMER modelling is relatively insensitive to the barrier height of the initial 1,5 H-shift (R1OO-15TS in Figure S4). The H-shift barrier needed to be lowered by 7 kcal mol^{-1} to yield a 2 % prompt 1,5 H-shift reaction even under the relatively low pressures of 100 Torr employed in the experiment. Such an error in the calculated barrier height is highly unlikely given the high level of theory employed which yields results in good agreement with the very recent results by Weidman et al.[7]

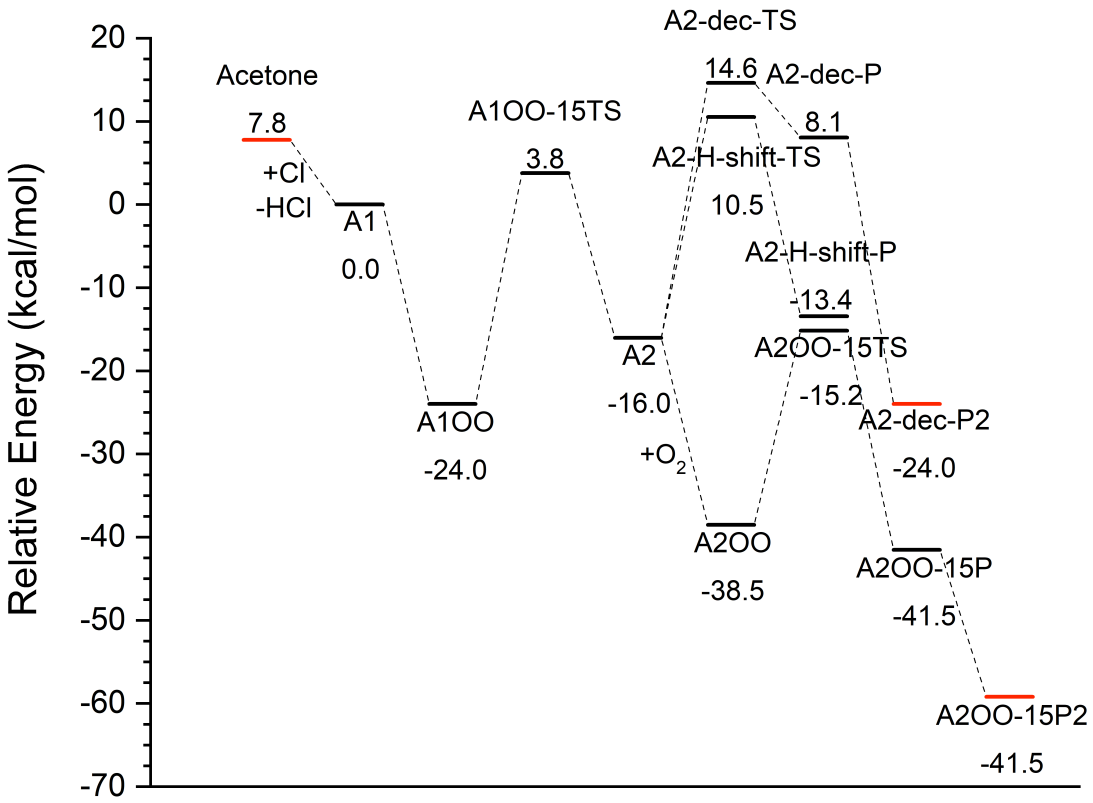

Figure S4. RO-CCSD(T)-F12a/VDZ-F12//ωB97X-D/aug-cc-pVTZ electronic energies with ωB97X-D/aug-cc-pVTZ ZPVE energetics of the lowest-energy conformers involved in the reactions outlined in Figure 11 in the main manuscript and used for the RRKM-ME modeling. The species in red correspond to those in brackets in Figure 11 in the main manuscript and are not explicitly modelled, but shown here for completeness.

III. Calculated Unimolecular Reaction Rate Coefficients

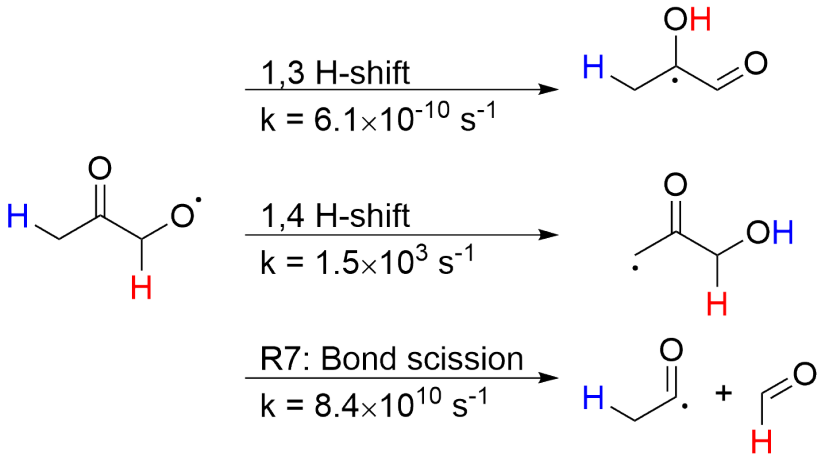

Figure S5. MC-TST rate ceefficient calculated using the approach by Møller et al.[8] at 298.15 K. The barrier for the bond scission (R7 in the main manuscript) is so low (3.77 kcal/mol) that the absolute rate constant is not reliable, but the reaction is very fast. Only the hydrogens that are involved in the H-shift reactions are shown explicitly.

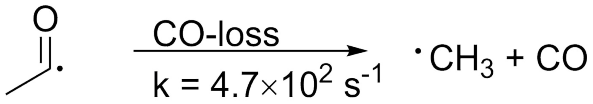

Figure S6. MC-TST rate coefficient calculated using the approach by Møller et al.[8] at 298.15 K.

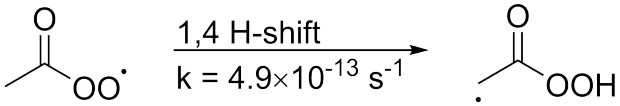

Figure S7. MC-TST rate coefficient calculated using the approach by Møller et al.[8] at 298.15 K.

IV. Kinetic Simulations of UV Absorption from Secondary Species

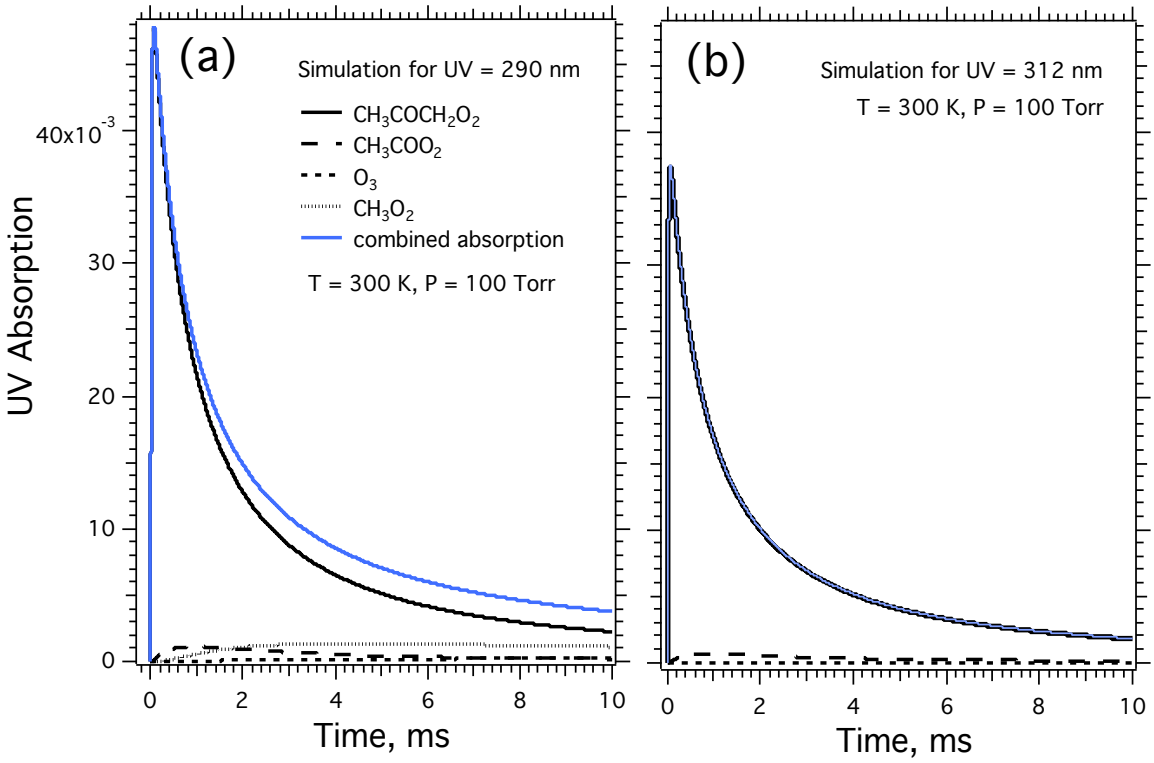

Figure S8. Simulation of the UV (a) λ = 290 nm and (b) λ = 312 nm absorption using fitted values derived in this work for the acetonylperoxy self-reaction. Concentrations were representative of typical experiments from this work. The combined absorption (blue) that would be observed in experiments represents concentrations of acetonylperoxy (black, solid), acetyl peroxy (black, long-dashed), ozone (black, short-dashed), and methyldioxy (black, dotted). The y-axis is shared for (a) and (b).

V. Additional 1/Abs vs. Time Measurements

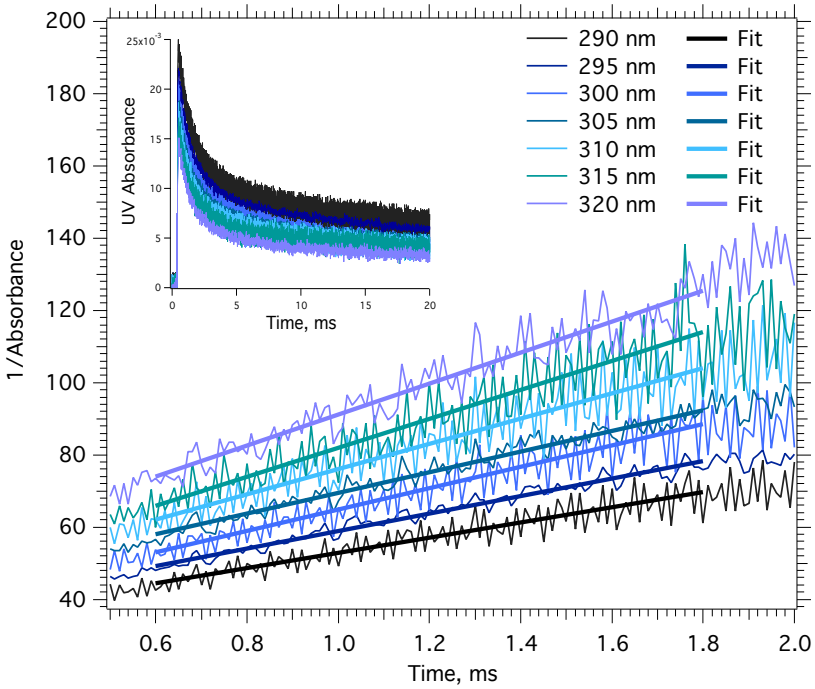

Figure S9. 1/Abs vs. time measurements obtained under conditions of no methanol and constant laser power and [Cl_2] to observe the acetonyl peroxy self-reaction. Each set of data shown in the inset for select λ = 290 – 320 nm was converted to 1/Abs and fit with a linear regression following pseudo-second order kinetics in the 0.6 – 2 ms range.

VI. FACSIMILE Kinetics Fitting

The FACSIMILE software package[9] performs non-linear least squares fitting on a set of reactions with parameters which include rate constants, initial concentrations, and absorption cross sections to time-dependent concentration data of one or more components involved in the mechanism, all of which is provided by the user. In addition, the user provides the expected standard error for the concentration data. A subset of the parameters can be allowed to vary to obtain a fit of the concentration data which can be visually compared to the actual data. In the work presented here, k_1, $k_{11,obs}$, $\sigma_{CH3C(O)CH2O2}$, and initial radical concentration were varied in the reaction scheme given in Table 1 of the main text. In addition, the resulting values of the varied parameters are output with 95% Confidence Intervals (95% CI). Furthermore, the residual sum

of squares (RSS) is also given which is compared to an expected range for this statistical parameter. If the RSS value falls outside the range, the standard error values need to be adjusted until it falls inside the range to obtain a "good" fit. A range of reasonable standard error values, which has to be discovered, will allow a "good" fit to occur.

The detection method for the IR (HO_2) is far superior to that of the UV [$CH_3C(O)CH_2O_2$] resulting in a significantly smaller standard error for the IR (~ ±0.3%) than the UV signal (~ ±15%). However, because the relative values of the standard errors input into FACSIMILE determines the relative weighting of the two curves in the fitting, using these standard errors resulted in very poor fits for the UV signal. Larger standard errors for IR (~1%) and smaller standard errors for UV (~5%) were found to not change the quality of the IR fit noticeably while greatly improving UV fit.

When fitting several parameters and more than one concentration curve, many "good" fits can be obtained resulting in a range of the desired varied parameters. Furthermore, the fits and the corresponding determined parameters can be sensitive to the initial values provided for these parameters. The method we employed in using the FACSIMILE software was to explore this range of parameters and standard errors that gave "good" fits to determine the best of these fits. The best fits were determined by small 95% CI total for all varied parameters coupled with a visual inspection of the fitted curve to the data showing a random distribution of the residuals. For the initial values for the varied parameters, we started with the currently recommended values using expected standard error values for the IR and UV signals. These initial fits resulted in improved values for the varied parameters that were then used to adjust the standard error values within a reasonable range to find low 95% CI. The resulting values were then used in an iterative fashion to find the final set of "best" fits. The range in the values of the fitted

parameters from the best fits (±2.5%) was usually greater than the 95% CI (0.5%) found in any one fit and is a better indicator of the uncertainty in these values due to fitting. Applying the Monte Carlo method of sampling the uncertainty in the parameters used in the overall mechanism with the new data revealed an increase in uncertainty for the rate constants determined to be approximately 4%; the uncertainty in these parameters was then increased from 2.5% to 4% for weighting purposes.

VII. Determination of equilibrium constant K_c(R14)

$$K_c(R14) = \frac{[HO_2 \bullet CH_3C(O)CH_3]}{[HO_2][CH_3C(O)CH_3]} \quad \text{(ES3)}$$

The method in Grieman et al.[10] assumes that the initial $[HO_2]$ (taken at time zero of the HO_2 decay) in the presence of acetone is $[HO_2]_{eq}$ because of the rapid establishment of the complex equilibrium (R14). The $[CH_3C(O)CH_3]_{eq}$ is in excess. The $[HO_2 \bullet CH_3C(O)CH_3]_{eq} = [HO_2]_0^* - [HO_2]_{eq}$ where $[HO_2]_0^*$ is the initial concentration of HO_2 with no acetone, $[HO_2]_0$, corrected for the reaction Cl + $CH_3C(O)CH_3$ (R3). The values of $[HO_2]_0$ and $[HO_2]_{eq}$ are determined by extrapolation of the fits to the $[HO_2]$ decay curves to t = 0 s at varying $CH_3C(O)CH_3$ concentrations shown in Figure S10.

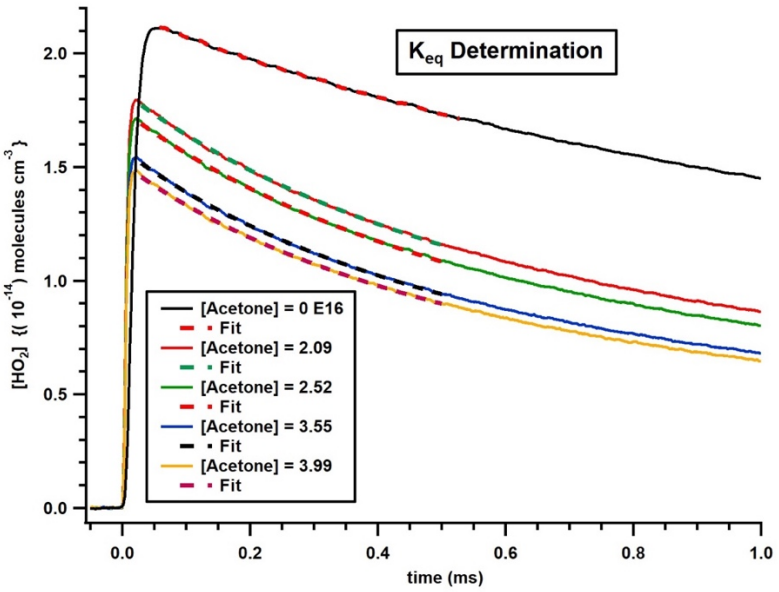

Figure S10: Determination of K_{eq}(R14) by extrapolation of the [HO_2] decay curve to t = 0.

VIII. Chaperone Effect from $HO_2 \bullet CH_3OH$

The results of fitting the data for $k_{11,obs}$ (cm^3 $molecule^{-1}$ s^{-1}) for the range $[CH_3OH]_0$ = 2.0 – 12 × 10^{15} molecules cm^{-3} gave a linear fit (Equation 2).

$$k_{11,obs}\,(T = 294\ K) = k_{11} + k''_M\,[CH_3OH]_0$$

$$= (1.7 \pm 0.2) \times 10^{-12} + (1.9 \pm 0.3) \times 10^{-29} \times [CH_3OH]_0 \qquad (E2)$$

where k''_M is the CH_3OH chaperone factor accounting for the increased HO_2 self-reaction rate due to the fast reaction with the complex (R12).

$$HO_2 + HO_2 \bullet CH_3OH \rightarrow H_2O_2 + O_2 + CH_3OH \qquad (R13)$$

Only a weak dependence on [CH_3OH] is observed with the values of $k_{11,obs}$ measured agreeing within the uncertainty of the JPL recommended value[35] for k_{11}, also shown in Figure S10.

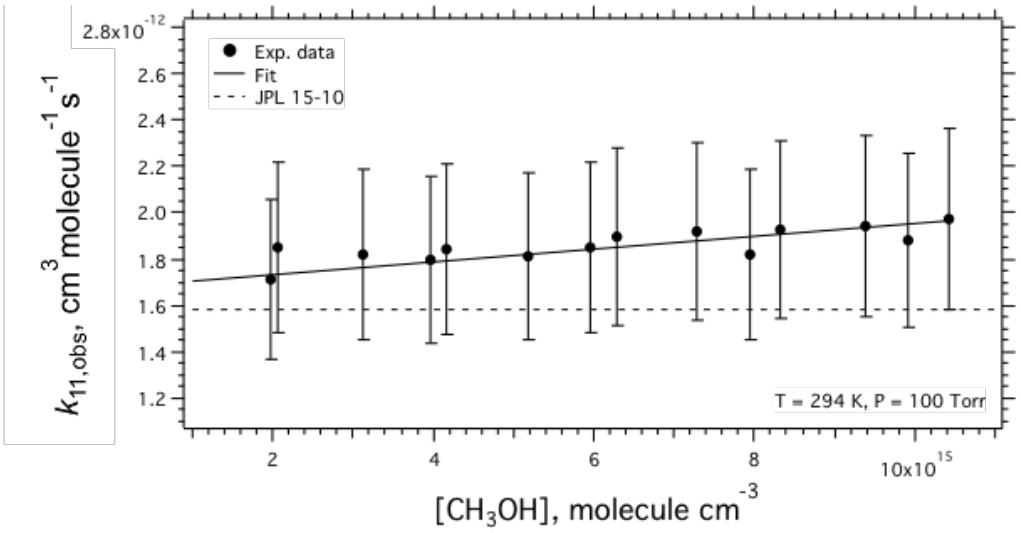

Figure S11. Experimentally determined values of $k_{11,obs}$ as a function of CH_3OH concentration. The fit (black line) was weighted by the uncertainties in each value. The dashed line represents the current recommended value for k_{11} in the JPL Data Evaluation.[2]

IX. Chaperone Effect from $CH_3C(O)CH_3$ on R1

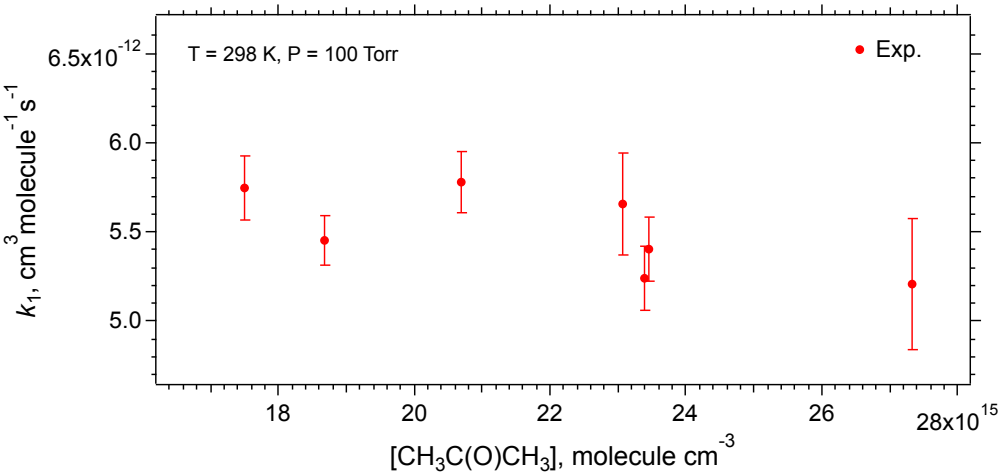

Figure S12. Experimentally determined values of k_1 as a function of $CH_3C(O)CH_3$ concentration.

REFERENCES

1. Gordon, I. E.; Rothman, L. S.; Hill, C.; et al. The HITRAN2016 Molecular Spectroscopy Database. *J. Quant. Spectrosc. Ra.* **2017**, *203*, 3-69.

2. Burkholder, J. B.; Sander, S. P.; Abbat, J. P. D.; Barker, J. R.; Huie, R. E.; Kolb, C. E.; Kurylo, M. J.; Wilmouth, D. M.; Orkin, V. L.; Wine, P. H., *Chemical Kinetics and Photochemical Data for Use in Atmospheric Studies, Evaluation No. 18*. JPL Publication 15-10: Jet Propulsion Laboratory, Pasadena, 2015.

3. Rissanen, M. P.; Eskola, A. J.; Nguyen, T. L.; Barker, J. R.; Liu, J. J.; Liu, J. Y.; Halme, E.; Timonen, R. S. $CH_2NH_2 + O_2$ and $CH_3CHNH_2 + O_2$ Reaction Kinetics: Photoionization Mass

Spectrometry Experiments and Master Equation Calculations. *J. Phys. Chem. A* **2014,** *118*, 2176–2186.
4. Barker, J. R.; Yoder, L. M.; King, K. D. Vibrational Energy Transfer Modeling of Nonequilibrium Polyatomic Reaction Systems. *J. Phys. Chem. A* **2001,** *105*, 796–809.
5. Hippler, H.; Troe, J.; Wendelken, H. J. Collisional Deactivation of Vibrationally Highly Excited Polyatomic-Molecules. 3. Direct Observations for Substituted Cycloheptatrienes. *J. Chem. Phys.* **1983,** *78*, 6718–6724.
6. Cuadros, F.; Mulero, A.; Cachadiña, J.; Ahumada, W. A New Procedure for Determining Lennard-Jones Interaction Parameters. *Int. Rev. Phys. Chem.* **2008,** *14*, 205–213.
7. Weidman, J. D.; Turney, J. M.; Schaefer, H. F. Energetics and Mechanisms for the Acetonyl Radical + O_2 Reaction: An Important System for Atmospheric and Combustion Chemistry. *J. Chem. Phys.* **2020,** *152*, 114301.
8. Møller, K. H.; Otkjær, R. V.; Hyttinen, N.; Kurten, T.; Kjaergaard, H. G. Cost-Effective Implementation of Multiconformer Transition State Theory for Peroxy Radical Hydrogen Shift Reactions. *J. Phys. Chem. A* **2016,** *120*, 10072–10087.
9. Curtis, A. R.; Sweetenham, W. P. FACSIMILE/CHEKMAT, H015 ed, v. 4.1.41; MCPA Software: Harwell, Oxfordshire, U.K. 1987.
10. Grieman, F. J.; Noell, A. C.; Davis-Van Atta, C.; Okumura, M.; Sander, S. P., Determination of Equilibrium Constants for the Reaction between Acetone and HO_2 Using Infrared Kinetic Spectroscopy. *J. Phys. Chem. A* **2011**, *115*, 10527–10538.